http://dx.doi.org/10.1016/j.ultrasmedbio.2013.12.022

● *Original Contribution*

THE FEASIBILITY OF MYOCARDIAL INFARCT VISUALIZATION USING ATRIAL KICK INDUCED STRAIN (AKIS) CONTRAST

BRETT BYRAM,*[1] HAN KIM,[†] LOWIE VAN ASSCHE,[†] PATRICK D. WOLF,* and GREGG E. TRAHEY*

*Department of Biomedical Engineering, Duke University, Durham, NC, USA; and [†]Department of Cardiology, Duke University Medical Center, Durham, NC, USA

Abstract—The most common mechanical measure of the heart integrates ventricular strain between end-diastole and end-systole in order to provide a measure of contraction. Here an approach is described for estimating a correlate to local passive mechanical properties. Passive strain is measured by estimating ventricular strain during atrial systole. During atrial systole the atria contract causing passive stretching in the ventricles from increased volume. This modification to traditional cardiac strain is here termed atrial kick induced strain (AKIS) imaging. AKIS imaging was evaluated in a canine ablation model of chronic infarct and a canine true chronic infarct model. AKIS images of ablation lesions were compared against acoustic radiation force impulse (ARFI) images and tissue blanching, and true chronic infarct AKIS images were compared against delayed enhanced-contrast magnetic resonance. AKIS images were made with 2-D and 3-D ultrasound data. In both studies, AKIS images and the comparison images show good qualitative agreement and good contrast and contrast-to-noise ratio. (E-mail: brett.c.byram@vanderbilt.edu)   © 2014 World Federation for Ultrasound in Medicine & Biology.

Key Words: Echocardiography, Cardiac elastography, Bayesian speckle tracking, Atrial kick, Prestretch, Active filling, AKIS, Elastography, Ultrasound.

INTRODUCTION

Echocardiography is ubiquitous in cardiac diagnostics and as a result, advances in ultrasound have the possibility to rapidly infiltrate clinical practice and quickly affect clinical decisions and subsequent outcomes. The best, recent example of this is the rapid adoption of tissue harmonic imaging. Another class of advanced methods in echocardiography with similar significant potential is mechanical measures and images of the heart. Mechanical measures of the heart can reasonably be divided into two categories based on whether the measure estimates functional or structural properties. These properties are correlated, but the correlation is not total so different information is expressed by the estimates of cardiac structural properties versus the quantification of functional dynamics. Cardiac dynamics are most commonly measured using strain (Urheim et al., 2000) or strain-rate (Heimdal et al., 1998) methods, but other functional methods showing promise include electromechanical wave imaging (Provost et al.,

2010). Quantification of cardiac dynamics through strain or strain-rate approaches is the mechanical measure closest to clinical adoption. However, these methods remain in the research sphere and are not yet generally recommended (Mor-Avi et al., 2011; Pellikka et al., 2007). Additionally, the useful diagnostic role of strain and strain-rate metrics have been questioned directly and indirectly because of lackluster results emerging from large clinical trials (Bonow et al., 2011; Cleland et al., 2011; Chung et al., 2008; Tanaka et al., 2010). In one case—the surgical treatment for ischemic heart failure (STICH) trial studying revascularization—the utility of any kind of imaging to guide the decision to revascularize the heart is called into question (Bonow et al., 2011; Velazquez, 2012), although specifically this trial only employs qualitative assessments of wall motion (Oh et al., 2012). In general, the lack of compelling empirical indicators delay widespread clinical adoption of functional cardiac metrics and images and do not allow for a definitive connection between well-characterized functional physiologic parameters of the heart and improved patient outcomes. The reason for the disconnect remains unclear, but may be because of inadequate algorithms, poor training, or a lack of useful connection between current (or any) mechanical measures and clinical outcomes. All

three possibilities have been hypothesized in the literature including the lack of connection between mechanical measures and clinical outcomes (Velazquez, 2012). Active mechanical measures are still pursued, probably, because conventional wisdom continues to advocate their utility.

The second category of mechanical measures attempt to estimate structural (or mechanical) properties. The following techniques are less mature in their application to the heart compared to strain or strain-rate imaging, but the methods have been studied extensively in other biological systems and show promise for cardiac applications in small studies on animals and humans. The methods include physiologically induced transverse wave propagation (Kanai, 2005), a variety of acoustically induced transverse wave propagation methods (Bouchard et al., 2009; Pislaru et al., 2009) and acoustically induced displacement methods (Hsu et al., 2007) (These methods are often converted to estimates of functional physiologic properties by considering the ratio between active and passive cardiac phases). In addition to structural stiffness, transverse wave propagation methods can be used to estimate anisotropic cardiac structure (Couade et al., 2011). Besides Kanai's method, the algorithms that image material parameters have only been demonstrated *in vivo* as part of clinically invasive protocols. We propose a modification to cardiac strain for obtaining mechanical information of the heart transthoracically.

Our approach uses the stretch induced in the ventricles from atrial contraction to form images correlated to the relaxed mechanical properties of the heart. In order to distinguish the mechanical properties measured in this modification to properties measured by typical strain methods the proposed approach is referred to as atrial kick induced strain (AKIS) imaging.

Others have recently quantified the strain induced in the ventricles during atrial contraction. Williams et al. (2005) studied strain during active filling as a possible correlate to regional exercise induced ischemia (Williams et al., 2005). Zwanenburg et al. (2005) studied the effect of AKIS on the timing and amount of ventricular contraction (Zwanenburg et al., 2005). Jasaityte et al. (2013) demonstrated that the stretch during atrial contraction combined with systolic strain correlates well to the inotropic state of the left ventricle (Jasaityte et al., 2013). Here, we demonstrate the possibility of using AKIS as a mechanism for non-invasively visualizing passive mechanical stiffness variations in tissue. AKIS images can be made using strain style algorithms readily implemented on data acquired using transthoracic echocardiography. As a demonstration of the approach, we show that images of instantaneous ventricular strain during atrial systole, which correlates to mechanical stiffness, can differentiate healthy myocardium from chronic infarct or ablated tissue.

MATERIALS AND METHODS

Overview

Atrial kick induced strain imaging creates contrast in the ventricles using atrial contraction. Atrial contraction results in an additional bolus of blood injected into the ventricles by the atria during the period of atrial systole, which usually accounts for 10% of the blood volume but can account for up to 40% at high heart rates (Klabunde, 2004). The small, but rapid increase in volume introduces a slight stretching of the ventricle to accommodate the extra fluid. The contrast in this new method comes from differences in diastolic stiffness (or compliance) of the heart. It is hypothesized that in regions where the organ is stiffer, such as infarcted tissue, the strain—instantaneous or accumulated—induced from the rapid volume change is less than in regions where viable myocardial tissue is present regardless of its functional behavior. For the initial realization of the algorithm, images are made based on the instantaneous strain between two frames 20 ms after the peak of the electrocardiogram's p-wave. This modification stands in contrast to traditional cardiac strain, which focuses on the cumulative strain during the entirety of ventricular systole.

Two experiments were conducted to demonstrate AKIS imaging. First, a study was conducted to visualize ablation lesions in open-chested dogs (N = 3) with 2-D and 3-D realizations of AKIS images compared against 2-D acoustic radiation force impulse (ARFI) imaging and tissue blanching. 2-D ARFI images of ablation have been previously validated against histology, and tissue blanching is a known result of ablation that can be used to assess whether ablations where transmural during an open-chest preparation. These methods will serve as a gold standard to assess ablation lesion location and size (Chik et al., 2012; Eyerly et al., 2010). When possible the ablation lesions were formed from the right ventricle chamber in order to better model the development of infarcted tissue. Ablation lesions have been used previously as a model for myocardial infarct in rats (Antonio et al., 2009).

The second study aimed to visualize chronic myocardial infarcts in a transthoracic canine model (N = 3) using AKIS images formed from 3-D ultrasound data. The gold standard for myocardial infarct visualization is delayed enhanced-contrast magnetic resonance (de-CMR) (Kim et al., 1999; Pennell et al., 2004; Simonetti et al., 2001), which will be used as the point of comparison for the AKIS images.

All studies were conducted in compliance with the Duke Institutional Animal Care & Use Committee.

Motion estimation

The cardiac motion is estimated using Bayesian speckle tracking (Byram et al., 2013a, 2013b). The

Bayesian speckle-tracking algorithm was implemented in 2-D or 3-D based on the dimensionality of the data set. The algorithm takes advantage of Bayes' Theorem, which for the purposes here can be expressed as

$$p_{\overrightarrow{m}}\left(\overrightarrow{\tau_0}|s_1(\overrightarrow{x}), s_2(\overrightarrow{x})\right) = \frac{p_{\overrightarrow{m}}\left(s_1(\overrightarrow{x}), s_2(\overrightarrow{x})|\overrightarrow{\tau_0}\right)p_{\overrightarrow{m}}\left(\overrightarrow{\tau_0}\right)}{\int p_{\overrightarrow{m}}\left(s_1(\overrightarrow{x}), s_2(\overrightarrow{x})|\overrightarrow{\tau_0}\right)p_{\overrightarrow{m}}\left(\overrightarrow{\tau_0}\right)d\overrightarrow{\tau_0}}. \tag{1}$$

In the eqn (1) $s_1(\overrightarrow{x})$ and $s_2(\overrightarrow{x})$ are the two N-dimensional signals separated by time, $\overrightarrow{m}$ references the kernel center, and $\overrightarrow{\tau_0}$ is the displacement vector. The likelihood function, $p_{\overrightarrow{m}}(s_1(\overrightarrow{x}), s_2(\overrightarrow{x})|\overrightarrow{\tau_0})$ for the Bayesian algorithm has been described by Byram et al. (2013a) and is

$$p_{\overrightarrow{m}}\left(s_1(\overrightarrow{x}), s_2(\overrightarrow{x})|\overrightarrow{\tau_0}\right) \propto \exp\left[\frac{\rho_{\overrightarrow{m}_{max}}}{\alpha\left(1-\rho_{\overrightarrow{m}_{max}}\right)}\rho_{\overrightarrow{m}}\left(\overrightarrow{\tau_0}\right)\right], \tag{2}$$

where $\rho_{\overrightarrow{m}}(\overrightarrow{\tau_0})$ is the N-dimensional normalized cross-correlation function between signals $s_1(\overrightarrow{x})$ and $s_2(\overrightarrow{x})$, and the α term is a scaling factor determined empirically from the kernel size (Byram et al., 2013a).

The prior probability, $p_{\overrightarrow{m}}(\overrightarrow{\tau_0})$ for the Bayesian implementation described here is a Gaussian distribution with a constant variance. The fixed Gaussian prior is a pragmatic assumption for computational efficiency, but it has been previously demonstrated that only small amounts of additional information provided by Gaussian distributed prior probabilities can result in displacement estimates surpassing traditional limits described by the Cramer-Rao bound (Byram et al., 2012). The means for the prior distributions are dynamic, determined by adjacent estimates. Specifically, the information is propagated in a manner similar to the method described by Chen et al. (2009, 2010). Initially, at least five seed positions are manually selected to be evenly distributed throughout the ventricle (volume data set seed positions are only placed in the central elevational slice). At the seed positions, the displacement is estimated using a large kernel, a large search region, and a non-informative prior distribution (a uniform probability density). The displacements of the large seed kernels are then used to estimate displacements with a smaller kernel at the same positions. The prior for the small kernel estimate is a Gaussian distribution with fixed variance and mean equal to the large kernel displacement. Prior probabilities are propagated from the initial seed locations based on estimation quality—quantified by the maximum normalized cross-correlation value of previous estimates. Displacement prior probabilities are propagated until all displacements are estimated.

The final displacements are estimated from the posterior distribution using the maximum *a posteriori* estimator, which is

$$\widehat{\overrightarrow{\tau_0}} = \underset{\overrightarrow{\tau_0}}{\text{argmax}}\ p_{\overrightarrow{m}}\left(\overrightarrow{\tau_0}|s_1(\overrightarrow{x}), s_2(\overrightarrow{x})\right), \tag{3}$$

which was further refined using parabolic subsample estimation (Céspedes et al., 1995).

Although only axial displacements will be used to calculate the final instantaneous strain results, displacements are estimated in all the available dimensions to decrease the Cramer-Rao bound and to decrease decorrelation from motion in lateral and elevational dimensions (Walker and Trahey, 1994).

Strain estimation and image formation

Cardiac strain estimation is a particular challenge compared to strain estimation in other static elastography problems. In most static elastography problems, tissue displacement is induced along the axial axis of the transducer so images of axial strain often create sufficient proxies for tissue stiffness. In contrast, relevant cardiac displacements occur in all directions regardless of whether the motion is active or passive, which means that important motion components are imposed on the point spread function's lateral and elevational dimensions. Displacements along these dimensions of the ultrasound beam have significantly higher displacement estimation jitter (or noise power) than in the axial dimension. Lubinski et al. (1996) demonstrated that noise power in the lateral and elevational dimensions is $40(f/\#)^2$ times higher than in the axial dimension (Lubinski et al., 1996). The anisotropy of the noise power may be tolerable in shallow low $f/\#$ imaging scenarios but becomes problematic for echocardiography, where in a realistic $f/5$ image configuration the noise power in the lateral and elevational displacements will be 1000 times greater. Additionally, the strain estimation process amplifies the noise increasing the importance of using only the best motion estimates (Varghese and

Ophir, 1997). One solution to this problem is to use an apical view of the left ventricle. Using this view, the longitudinal axis of the left ventricle aligns well with the axial dimension of the acoustic coordinate system allowing for low noise estimates of cardiac longitudinal strain. Although longitudinal strain is the simplest to estimate, there is interest in measures of circumferential and radial strain and in estimates of cardiac strain from other views. Other imaging views of the heart can be used, but the meaning of purely axial displacements and strains becomes location specific, complicating interpretation. The solution is to use the full 2-D or 3-D displacement vector to convert displacements from the ultrasound coordinate system into the cardiac coordinate system (Zervantonakis et al., 2007); however, this approach does not avoid the challenge of poor displacement estimates in azimuthal dimensions.

Another possible approach to the challenge of estimating cardiac strains is to consider an angle invariant strain metric. The concept of an angle invariant strain metric resembles the concept of tensor invariants, which are constant regardless of coordinate system and are often exploited in mechanics. In the case here, our angle invariant metric is not a general tensor property and is much more limited, but still very useful, for the purpose of displaying the instantaneous strain during atrial kick. Additionally, for the case of cardiac strain, the angle invariant metric would ideally depend only on axial displacement derived strains. Here, we demonstrate an angle invariant strain metric, and then we show an *ad hoc* modification so that the strain metric only depends on axial displacements. The angle invariant strain metric can be derived by first considering the rotation of the strain tensor from the cardiac coordinate system into a Cartesian coordinate system,

$$
\begin{bmatrix} S_{xx} & S_{xy} & S_{xz} \\ S_{yx} & S_{yy} & S_{yz} \\ S_{zx} & S_{zy} & S_{zz} \end{bmatrix} = \begin{bmatrix} \mathrm{Cos}\,(\theta) & -\mathrm{Sin}\,(\theta) & 0 \\ \mathrm{Sin}\,(\theta) & \mathrm{Cos}\,(\theta) & 0 \\ 0 & 0 & 1 \end{bmatrix}
$$
$$
\times \begin{bmatrix} S_{RR} & S_{R\theta} & S_{RZ} \\ S_{\theta R} & S_{\theta\theta} & S_{\theta Z} \\ S_{ZR} & S_{Z\theta} & S_{ZZ} \end{bmatrix} \begin{bmatrix} \mathrm{Cos}\,(\theta) & \mathrm{Sin}\,(\theta) & 0 \\ -\mathrm{Sin}\,(\theta) & \mathrm{Cos}\,(\theta) & 0 \\ 0 & 0 & 1 \end{bmatrix},
$$
(4)

where R, θ and Z are respectively the radial, circumferential and longitudinal dimensions of the cardiac coordinate system, and x, y and z are the local Cartesian coordinate system serving as an effective simplification of the acoustic coordinate system, where x, y and z correspond to the axial, lateral and elevational axis. This description of the acoustic coordinate system differs from most conventions, but does not create any fundamental changes. The appropriateness of this transformation depends on how well the transducer is aligned in a true short-axis view, although other probe alignments and subsequent transformations produce the same result. Additionally, we make several simplifying assumptions. First, we assume that sufficiently far from the apex, the ventricle can be approximately modeled as a thick cylinder, and second we assume that the heart is linearly elastic and isotropic. Of course, these are gross simplifications, but the assumptions allow us to conceptualize a simple description of the cardiac response to the atrial kick. Under these assumptions the circumferential and radial strains are

$$
S_{\theta\theta} = \frac{\sigma_{\theta\theta}}{E} - \nu\frac{\sigma_{RR}}{E} - \nu\frac{\sigma_{zz}}{E}
$$
$$
= \frac{r_i^2 p_i}{(r_o^2 - r_i^2)E}\left(\left(1 + \frac{r_o^2}{R^2}\right) - \nu\left(1 - \frac{r_o^2}{R^2}\right) - \nu\right)
$$
(5)

and

$$
S_{RR} = \frac{\sigma_{RR}}{E} - \nu\frac{\sigma_{\theta\theta}}{E} - \nu\frac{\sigma_{zz}}{E}
$$
$$
= \frac{r_i^2 p_i}{(r_o^2 - r_i^2)E}\left(\left(1 - \frac{r_o^2}{R^2}\right) - \nu\left(1 + \frac{r_o^2}{R^2}\right) - \nu\right),
$$
(6)

where r_i and r_o are the inner and outer radius of the ventricle, R is the radial location within the heart, p_i is the pressure on the endocardial surface from the blood, and E and ν are the mechanical properties Young's modulus and Poisson's ratio, respectively. Under these assumptions and assuming tissue incompressibility, it can be shown that the quantity

$$
|S_x| = \sqrt{S_{xx}^2 + S_{yx}^2 + S_{zx}^2}
$$
$$
= \frac{3 p_i r_i^2 r_o^2}{2 E R^2 (r_o^2 - r_i^2)},
$$
(7)

is angle invariant, proportional to the filling pressure and inversely proportional to the tissue's stiffness, however, there is a dependency on radial position, which will be less than a factor of two in human hearts. Unfortunately, one needs displacements along all three axes to calculate $|S_x|$ because the shear strain is defined as

$$
S_{ij} = \frac{1}{2}\left(\frac{\partial u_i}{\partial j} + \frac{\partial u_j}{\partial i}\right).
$$
(8)

To avoid this, terms in eqn (8) are ignored if they require azimuthal displacements so that only axial displacements are used. Based on this modification the strain metric used to form AKIS images is

$$
|S_x| = \sqrt{\left(\frac{\partial u_x}{\partial x}\right)^2 + \left(\frac{\partial u_x}{\partial y}\right)^2 + \left(\frac{\partial u_x}{\partial z}\right)^2}.
$$
(9)

Strain metric components are estimated from the displacement estimates using a least squares fit of displacements to a line (or plane), with the various slopes representing strain estimates (Kallel and Ophir, 1997).

Image masking

Before making the final instantaneous strain and ARFI images the non-myocardial portions of the images were masked. When possible the images were masked automatically using a modified version of the algorithm described by Nillesen et al. (2007). First, the k-means clustering algorithm was used with three intensity bins, and the middle intensity bin was used for the initial mask. Second, the localized deformable contour algorithm proposed by Lankton and Tannenbaum (2008) is used instead of a global contour. Any significant error in the masking was corrected by hand so the automatic segmentation should not significantly affect the results.

ARFI image formation

ARFI images are formed using an approach consistent with the methods previously validated against histology (Eyerly et al., 2010) with two small deviations to reflect the increased sophistication of ARFI imaging. First, a better autocorrelation method for displacement estimation is used (Loupas et al., 1995), and second, a better motion filter using an extrapolative fit of only displacement estimates of the physiologic motion measured before the ARFI push is used (Giannantonio et al., 2011). One additional modification to the method was to use the first displacement estimate after the ARFI pushing pulse to create ARFI images. This has the benefit of not magnifying the size of the lesion at the cost of decreasing the ARFI contrast (Nightingale et al., 2006).

Open-chested experimental validation

The open-chested validation study was performed on three canine subjects. The subjects underwent an open-chest preparation. For these dogs, ablation lesions (radiofrequency [RF] ablations or cryoablations) were made in the right ventricle and used as a model for myocardial infarct. When possible the ablation lesions originated on the endocardial layer to mimic the expected pattern of infarct growth. (In one case, the RF ablation was not placed on the endocardium because it was not feasible for the specific experimental situation. The RF-ablation lesion originated from the epicardial wall of the heart.) RF-ablation lesions were made using a Stockert 70 Generator and a NaviStar mapping/ablation catheter (Biosense Webster, Inc., Diamond Bar, CA, USA). For the canine subject with the epicardial ablation lesion the ablation catheter was an 8 French
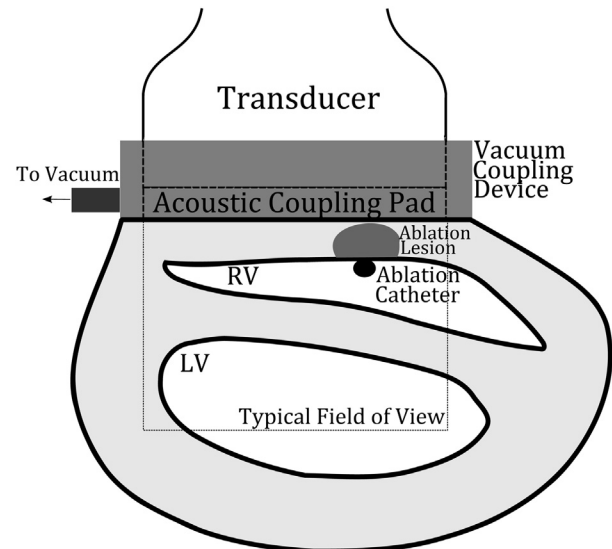
Fig. 1. An example of the relative orientation of the transducer, the vacuum coupling device, the RF-ablation catheter and the lesion are shown. The transducer was placed so that the ablation lesion was within the field of view and good suction could be achieved with the vacuum coupling device. Generally, the position of the transducer did not align with traditional cardiac views. In this configuration data were acquired only to a short depth and usually only the septal portion of the left ventricle was acquired.

SteeroCath (Boston Scientific, Natick, MA, USA) connected to a Model 8002 RFA generator (Cardiac Pathways, Sunnyvale, CA, USA).

In one of the canine subjects, cryoablation lesions were also formed and imaged. The cryoablation lesions were formed only on the epicardial layer because a cryoablation catheter was not available. The cryoablation lesions were made using a Brymill Cry-Ac Tracker with a 3-mm Mini Probe (Brymill Cryogenic Systems, Ellington, CT, USA). A diagram of the experimental setup is shown in Figure 1.

For this study, the canines were imaged using 2-D and 3-D ultrasound. The 2-D data were acquired using a SONOLINE Antares ultrasound system and VF10-5 linear array transducer (Siemens Healthcare, Ultrasound Business Unit, Mountain View, CA, USA). The 2-D data were acquired with the transducer fixed to the heart surface using a vacuum coupling device described previously by Hsu et al. (2009) that minimizes lateral and elevational motion. The 2-D data for strain imaging were acquired in conjunction with a sequence of ARFI images. The data set consisted of 14 ARFI image frames at 10 Hz followed by 200 B-Mode frames at 134 Hz. For one data set—the data set with the ablation lesion originating from the epicardial surface of the heart—the ARFI images were acquired at 14 Hz and the B-Mode data were acquired at 168 Hz, and the VF7-3 transducer was used.

The data were acquired at baseband with 4-to-1 parallel receive beamforming and acquisition.

The 3-D data were acquired using a Siemens Acuson SC2000 imaging system and a 4 Z1 C matrix array transducer (Siemens Healthcare Sector). The data were acquired in a 30-to-1 parallel receive beam configuration at baseband (Byram et al., 2010). The 3-D open-chested data were acquired at volume rates between 103–127 Hz based on experimental imaging constraints. Because the data were acquired on an open-chested canine, a water path was introduced between the transducer and the heart. The water path functioned as a standoff to position the transducer about 8 cm (the focal depth) above the heart.

The 2-D and 3-D ultrasound data used to create the instantaneous strain images were re-modulated and turned into RF data and then used to estimate cardiac motion in the manner described. The experimental parameters for the 2-D processing are shown in Table 1, and the experimental parameters for the 3-D processing are shown in Table 2.

Contrast and contrast-to-noise ratio (CNR) image metrics are calculated on the AKIS images of the ablation lesions. The image metrics are calculated on unmodified AKIS images (*i.e.,* the data has not been thresholded). Contrast is calculated using $C = \frac{\mu_{background} - \mu_{lesion}}{\mu_{background}}$. The CNR is calculated using $CNR = \frac{|\mu_{background} - \mu_{lesion}|}{\sqrt{\sigma_{background}^2 + \sigma_{lesion}^2}}$.

Chronic infarct experimental validation

The second study consisted of three dogs with chronic infarcts. The ligation preparation for each dog was performed more than a year before the time of ultrasonic imaging allowing sufficient time for the infarcts to become chronic. At the time of the ultrasound data acquisition, the dogs weighed 22.7, 27.9 and 30.3 kg. The canines were imaged with the Siemens Acuson SC2000 (Siemens Healthcare Sector). The data were acquired at volume rates between 160–240 Hz based on experimental constraints. In order to obtain volumes at such high rates the lateral and elevational fields of view as well as the imaging depth were reduced to produce the fastest volume rate possible for a given dog. The fields of view in the lateral and elevational dimensions were between 60°–80° and 10°–15°, respectively, based on the experimental specifics of each canine subject.

The canine subjects were lightly sedated before the ultrasound image sequences were acquired. Two canine subjects were given IV Diazepam (.2 mg/kg) and Butorphanol (.1 mg/kg), while the remaining canine subject was given IV Midazolam (.2 mg/kg) and Butorphanol (.2 mg/kg); all doses were at the discretion of the attending veterinarian. The canines were unconstrained during the procedure and allowed to roam freely between acquisitions.

The de-CMR images were acquired for each canine subject before the ultrasonics exams. Before MR data acquisition, the canines were anesthetized with sodium pentobarbital and then intubated. During the MR sequence, the canines were under anesthesia with isoflurane.

The volumetric data were remodulated before processing. The experimental parameters are shown in Table 2. Image metrics were not calculated on the

Table 2. Parameters for the 3-D infarct study

Experimental parameters	
Center frequency	2.8 MHz
Baseband sampling frequency	2.5 MHz
Parallel receive beams (lateral)	5
Parallel receive beams (elevational)	6
Signal interpolation (axial)	16
Signal interpolation (lateral)	4
Signal interpolation (axial)	4
Interpolation type	Linear
Large kernel size (axial)	17 Nyq.
Large kernel size (lateral)	2 Nyq.
Large kernel size (elevational)	2 Nyq
Small kernel size (axial)	11 Nyq.
Small kernel size (lateral)	1 Nyq.
Small kernel size (elevational)	1 Nyq.
Prior σ (axial)	0.230
Prior σ (lateral)	0.215
Prior σ (elevational)	0.191
Axial kernel Overlap (small kernel only)	91%
Strain kernel size (axial)	7 Nyq.
Strain kernel size (lateral)	3 Nyq.
Strain kernel size (elevational)	3 Nyq.

Nyq. = Nyquist.
The Nyquist (Nyq.) unit is half of the transform predicted resolution volume.

Table 1. Parameters for the 2-d ablation lesion study

Experimental parameters	
Center frequency	8 MHz
Baseband sampling frequency	8.9 MHz
Parallel Receive Beams (lateral)	4
Signal Interpolation (axial)	16
Signal Interpolation (lateral)	4
Interpolation method	Linear
Large kernel size (axial)	17 Nyq.
Large kernel size (lateral)	5 Nyq.
Small kernel size (axial)	13 Nyq.
Small kernel size (lateral)	5 Nyq.
Prior σ (axial)	0.225 Nyq.
Prior σ (lateral)	10.4 Nyq.
Axial kernel overlap	92%
Strain kernel size (axial)	20 Nyq.
Strain kernel size (lateral)	10 Nyq.

Nyq. = Nyquist.
The Nyquist (Nyq.) unit is half of the transform predicted resolution volume.

Fig. 2. Example strain magnitude images are shown for the individual components of eqn (9) in Figures 2a–c and for the full axial strain magnitude in Figure 2d. The example shows the axial strain magnitude in a healthy short-axis view of a canine. The complete strain magnitude using all three dimensions has reduced angular dependency even without using the full shear strain.

AKIS images of chronic infarct because the infarct structure and boundaries can be complex.

RESULTS

Demonstration of the strain metric

First, before results are presented for the ablation and chronic infarct experiments, we demonstrate the utility of the instantaneous strain metric in a healthy short-axis image view of a canine. Figure 2 shows strain images created from each component of eqn (9) and an image of the full instantaneous strain magnitude. The figure shows that each component by itself maintains angular variations in strain, but when the magnitudes combine, they produce a uniform result. Additionally, the example shows that even though shear strains are not used to calcu-late the strain magnitude metric, the metric becomes less angle dependent.

Open-chested ablation visualization

The first ablation image examples are shown in Figure 3. Images are shown for 2-D ARFI and 2-D and 3-D AKIS. In this data set, the lesion originated on the endocardial surface of the heart and was transmural. The ARFI image by itself does not indicate a transmural ablation probably because of field of view limitations imposed by the ARFI push beam; however, tissue blanching was observed on the epicardial surface of the heart. The 2-D instantaneous strain data shows a lesion that is convincingly transmural. The first of the lower pair of images is the pre-ablation B-Mode and overlayed strain
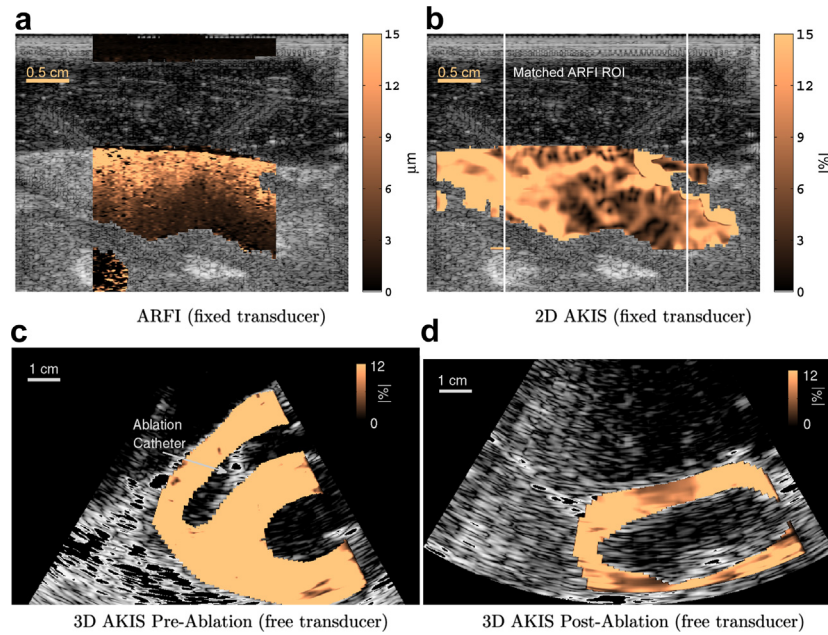
Fig. 3. Matched ARFI and 2-D and 3-D AKIS images of an ablation lesion are shown. The ARFI image, shown in Figure 3a, shows an ablation with poor definition in the axial dimension probably owing to a short depth of field. The 2-D AKIS image, Figure 3b, shows a low strain zone in the same position and of similar morphology as the ARFI lesion. An AKIS image created from volumetric data pre-ablation is shown along with an image after the ablation in Figure 3c and d, respectively. The AKIS images show a lesion of nearly the same size between 2-D and 3-D cases and suggest the observed transmurality better than the ARFI image.
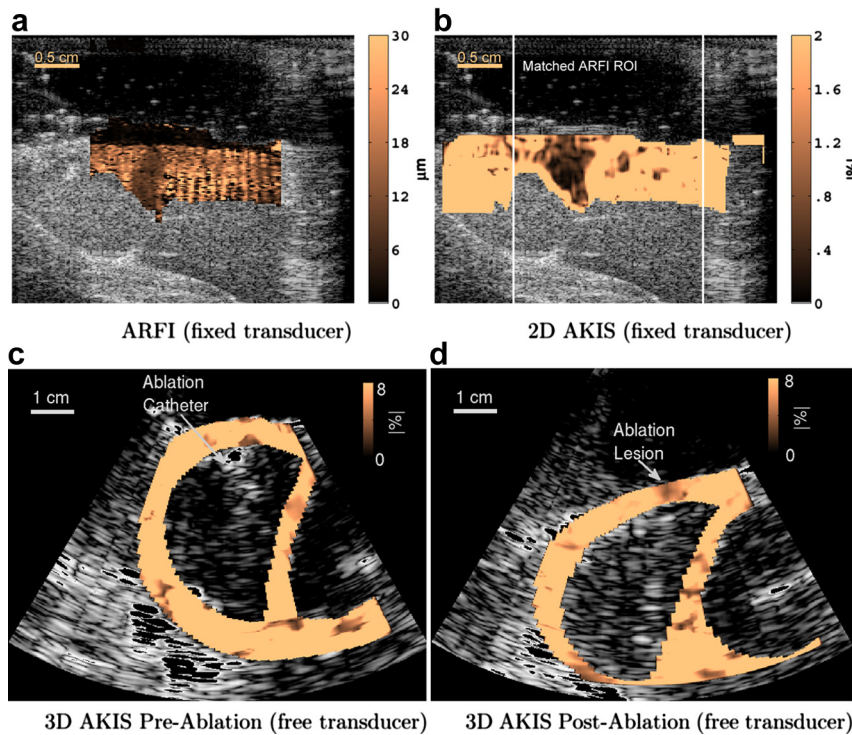
Fig. 4. A small stiff lesion formed using RF-ablation is shown. The figures shows ARFI (Fig. 4a) and 2-D (Fig. 4b) and 3-D (Figs. 4c,d) strain images. In all images, there is evidence of a lesion. There is high correlation between the ARFI image and the 2-D AKIS image. The lesion is difficult to see in the strain image derived from 3-D B-Mode, but there is a noticeable difference in the strain at the tip of the ablation catheter before and after the ablation occurred.
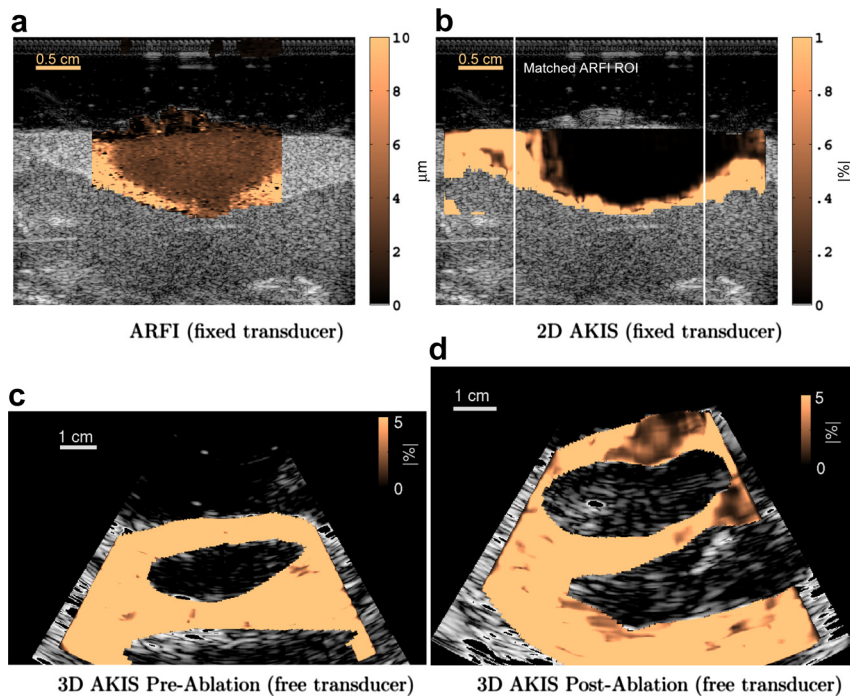
Fig. 5. 2-D and 3-D visualizations of a cryoablation lesion using ARFI and AKIS images are shown. Figures 5a,b shows the 2D ARFI and AKIS images respectively, and Figures 5c,d show pre- and post-ablation 3D AKIS images. The lesion is clearly visible in all three image types. Additionally, the swelling induced in the myocardium from the cryoablation makes it easy to register the 2-D and 3-D images.

image. The image generally shows homogeneous strain (when saturated to the level used for the ablated case). The ablation catheter is visible in the image. The second 3-D AKIS image shows post-ablation myocardium. The ablation is clearly transmural. This image appears to be the same size as the lesion visualized using 2-D strain. The 3-D AKIS image shows worse contrast compared to the 2-D AKIS image created with a fixed transducer.

The second example RF-ablation visualization case is shown in Figure 4. The lesion for this case was small and could be manually palpated, but there was no visible evidence of an ablation lesion when viewing the epicardial surface of the heart. The ARFI and 2-D AKIS images for this set show generally well defined but small lesions. Although the lesion was not observably transmural, both the ARFI and instantaneous strain images show a lesion that spans the full thickness of the wall. The 3-D volumes were also used to create AKIS images. For the 3-D case, the lesion is hard to see except in the context that the lesion occurred at the end of the ablation catheter. In the pre-ablation data, the tissue at the tip of the ablation catheter has high strain while in the post-ablation image the strain magnitude is low at the tip of the ablation catheter. This set of images likely provides an approximate lower bound on visualizable lesion size for the 3-D imaging parameters used here.

In Figure 5, results from imaging a cryoablation are shown. (This particular data set is useful because the

cryoablation is visible as a swelling in the myocardial wall, which makes it easy to register between the 2-D and 3-D B-Mode images.) This figure shows both ARFI and 2-D and 3-D AKIS images that clearly demarcate the lesion. The ARFI and 2-D AKIS images show some subtle differences in the boundary at the bottom of the lesion, but otherwise match closely. The AKIS image derived from 3-D ultrasound data also shows differences along the boundary, but the size and location match well.

Image metrics for all the lesions used in the study are shown in Table 3. Contrast and CNR are shown for the 2-D and 3-D cases. The initial trend appears to be that the 2-D imaging scenario has better contrast relative to 3-D data derived AKIS images. The CNR numbers appear comparable between 2-D and 3-D. There is one data set (dog #3) in Table 3 with poor 2-D metrics. This data set is the same one used in Figure 3, which also made a poor 2-D ARFI image. There may be something about this particular study that results in poor 2-D images. For dog #1, shown in Table 3, a volumetric data set was not available.

Image metrics are also displayed through time for the 2-D data sets in Figure 6. The figure shows the metrics from individual frames as well as accumulated frames for the period during atrial contraction as well as the traditional period during ventricular systole. This figure also shows that there is not a strong peak for optimal AKIS

Table 3. Ablation lesion contrast and CNR estimates

	Contrast		CNR	
Lesion ID	2-D	3-D	2-D	3-D
Dog #1 (RF)	0.7526	N/A	2.0591	N/A
Dog #2 (RF)	0.8442	0.7678	1.2572	1.3748
Dog #2 (Cryo)	0.9787	0.8634	1.469	1.410
Dog #3 (RF)	0.1197	0.5747	0.0815	2.7336

RF = radio frequency; Cryo = cryoablation; CNR = contrast-to-noise ratio.

instantaneous contrast or CNR. The 20 ms that was chosen corresponds to approximately 0.1 in the arbitrary scaled time units used in the graphs.

Chronic infarct visualization

Results are now shown for the second experimental study. This study aimed to visualize chronic infarcts using instantaneous strain derived from raw 3-D B-Mode ultrasound. The study examined three different dogs and compared the ultrasound strain images against de-CMR images. Two of the canine subjects resulted in AKIS images that correlated well with the de-CMR images, but the third subject had B-Mode image quality that was too poor in every case to sufficiently distinguish the heart wall.

The first data set is shown in Figure 7. This figure shows data from two acquisitions of the first canine subject. Several matched de-CMR images are also shown

because the infarct for this dog was large and changed significantly from the base to the apex. The selected de-CMR slices were chosen based on qualitative similarities of the left ventricle's shape and dimensions in the B-Mode image. The de-CMR image displays infarcted tissue as bright pixels and viable myocardium as dark pixels. In the de-CMR images, the chambers also show up as bright pixels. In the MR image, the infarct is in the lateral wall (*i.e.,* the right side of the left ventricle away from the septum). The AKIS images show regions of low strain in the same location. The AKIS images may also show internal structure in the region of infarct that matches well with structure on the de-CMR images.

Results from the second dog are shown in Figure 8. These results show a B-Mode image, an AKIS image derived from 3-D ultrasound data and a de-CMR image. The data show general agreement with the position of the low strain regions of the AKIS image and the regions of infarct in the MR image. In the AKIS image, the low strain region appears to extend through the cardiac wall in some spots, which is not observed in the de-CMR images. This is likely because the full thickness of the cardiac wall is not captured due to the shallow position of the heart and the reduced lateral field of view. The field of view is decreased further when calculating the displacement and strain estimates. (This is not a problem when the heart is positioned deeper as in most clinical
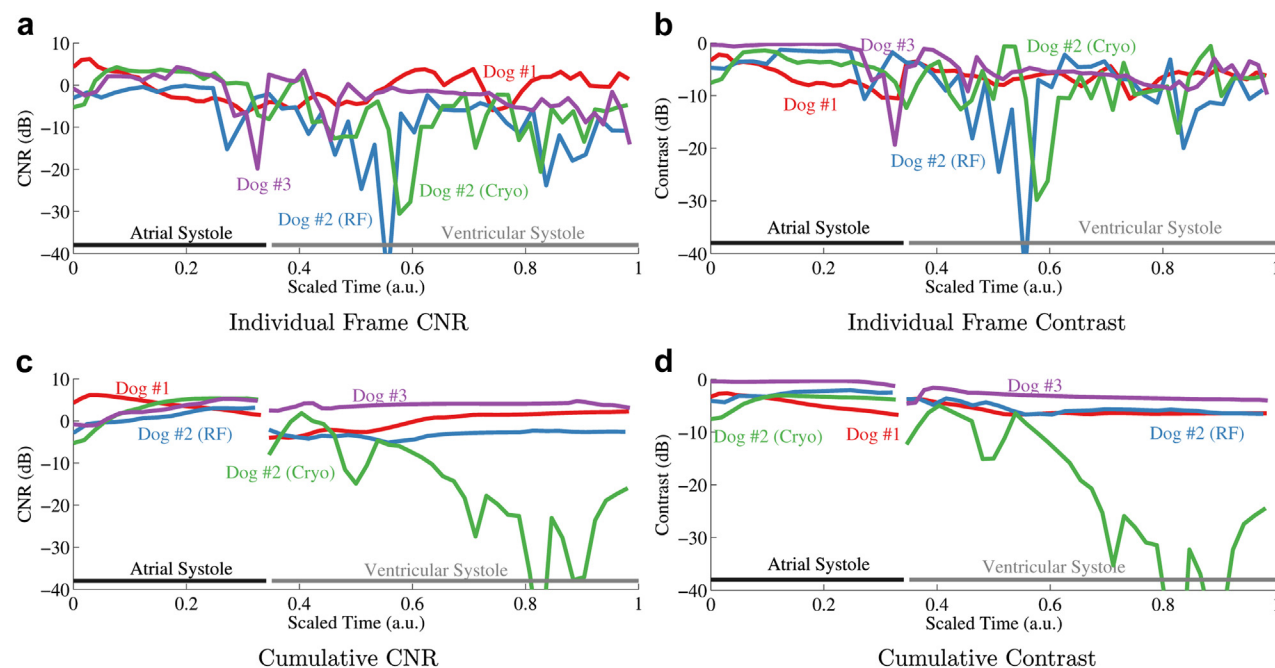
Fig. 6. Individual frame and cumulative CNR and contrast results are shown. Individual frame CNR and contrast are shown in Figures 6a and b, respectively, cumulative frame CNR and contrast are shown in Figures 6c and d, respectively. For the cumulative strain results, the strain frames are integrated from the start of the systolic period. Results are shown through atrial and ventricular systole. For these graphs the length of atrial systole and ventricular systole were normalized for easier comparison. The relative duration of atrial and ventricular systole were determined based on the median duration from the data.
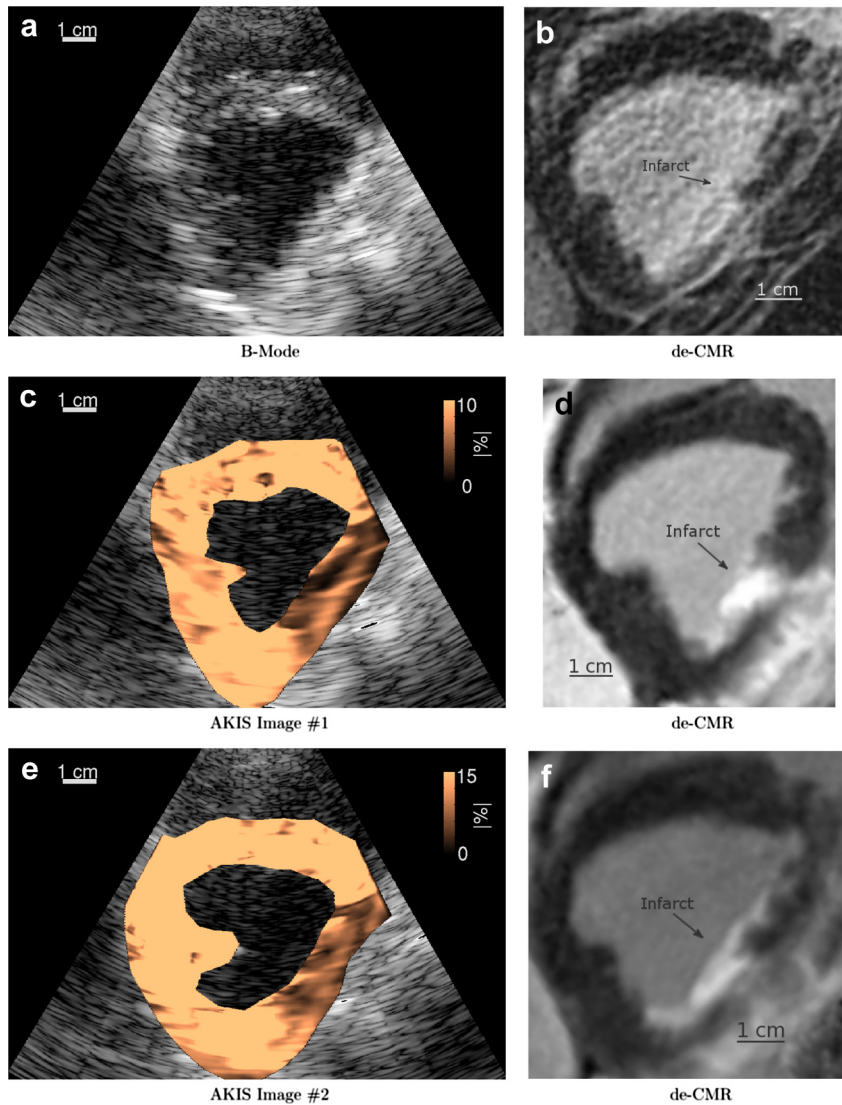
Fig. 7. AKIS and de-CMR images of a dog are shown. The AKIS images shown in Figures 7c and e were acquired one hour apart, and the canine was unconstrained during the duration of the study. The de-CMR images are shown in Figures 7b,d, and f on the right side and represent longitudinal MR slices that possibly match the position of the B-Mode slice (Fig. 7a). This canine had a large infarct that changed significantly with depth. Several de-CMR slices are shown for a more fair comparison. The de-CMR images map the infarct to bright pixels and darker pixels to healthy myocardial tissue. The AKIS images show low strain regions in the same area as the de-CMR images. In some cases, the internal structure matches well between the de-CMR images and the AKIS images.

examinations.) In this case, only a single de-CMR slice is shown because the infarct is less dynamic across the relevant slices.

DISCUSSION

Both ablation lesions and chronic infarcts were reasonably visualized in a feasibility study investigating the imaging potential of atrial contraction induced strain in the ventricles. The results were best when images were made with 1-D linear array transducers vacuum coupled to the cardiac surface. The results from volumetric ultrasound data also visualized the ablated and infarcted tissue, but there was typically more noise present in the form of small low-strain regions where infarcted or ablated tissue was not known to be present.

While the results show the potential of AKIS as a mechanism for differentiating tissue stiffness and directly visualizing chronic myocardial infarct, there are clinically relevant scenarios when this approach would be contraindicated. Most significantly, hearts in atrial fibrillation could not be visualized in the proposed manner, and to a lesser extent, high heart rates may confound AKIS imaging. Additionally, the natural spatial
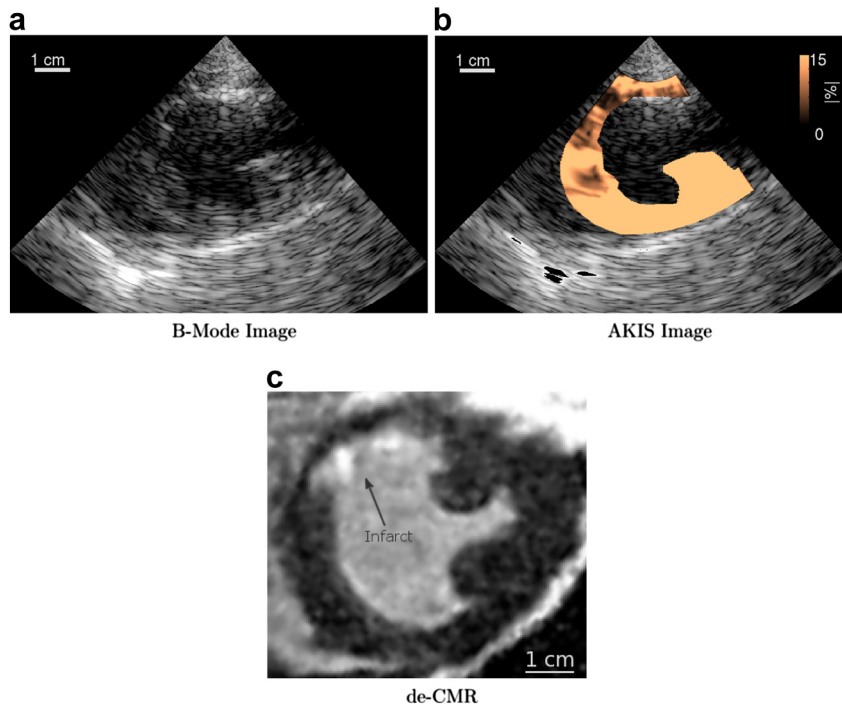
Fig. 8. AKIS and de-CMR images of a canine are shown in Figures 8b and c, respectively. The matching B-Mode image is shown in Figure 8a. The results shown in this figure show agreement in the position of the low-strain region in the strain image and the infarct region in the de-CMR image, but there is a discrepancy between the sizes of these zones. Some of this discrepancy may be due to masking part of the myocardium.

variability of the physiologically induced strain as reported by Zwanenburg et al. (2005) may also provide a limit on passive strain differentiation.

It may be tempting to infer from Figure 6 that AKIS images are higher quality in regard to contrast and CNR than traditional cardiac strain images. First, the purpose of AKIS imaging is not to make better images but rather to image different mechanical properties. Second, the initial study is small enough that this is still an open question and suggests at least three possible explanations. First, the process of accumulating strain along with estimation jitter acts as a low-pass filter to spatially smear the regional strain. In contrast, the AKIS results are formed from only two volumes without accumulation. Second, the displacement estimation scheme may be more optimized for displacements that occur during atrial contraction compared to displacements during ventricular systole. A third related hypothesis is that the volume rate used in this study may be more appropriate for estimating relaxed ventricular motion rather than active ventricular motion. All of these hypotheses are testable and immediately suggest future directions for a more thorough comparison.

Relative to the chronic infarcts studied here, infarcts can be significantly more complicated. Chronic infarcts may not stiffen, and lack of stiffening results in serious complications. Additionally, the period after an ischemic event may contain tissue that is edemic, infarcted, stunned and healthy. It is not clear whether these tissue states can be distinguished when they are all present simultaneously using AKIS. One possible solution is to combine the information from traditional functional myocardial strain with the new information from structural myocardial strain for more specific tissue identification.

Broadly, the purpose of AKIS is to provide a correlate to structural cardiac properties, but the specific results used to demonstrate the ability to estimate mechanical stiffness immediately suggests two clinical applications. First, as already discussed, the current gold standard for cardiac infarct visualization is de-CMR, unfortunately as a modality MR is expensive and slow. Additionally, cardiac MR has traditionally struggled with widespread clinical availability (Earls et al., 2002). An ultrasonic solution for direct (rather than inferred) infarct visualization (such as AKIS imaging) could result in less expensive and more accessible and rapid assessment of myocardial infarction. Second, the ablation lesion scenario was used as a model for infarct visualization. However, it seems clear that ablation lesion visualization is another possible application for AKIS imaging. AKIS imaging cannot be directly applied in the atria, but a similar strategy could be adopted to analyze the atria during their late reservoir phase when they are stretched. AKIS imaging should be directly

applicable to the growing number of catheter based ablation procedures being performed in the ventricles (Wissner et al., 2012).

Finally, the proposed method of using the atrial contraction as a method of inducing displacement gradients in the ventricles has been implemented using ultrasound, but any method that can measure displacements with sufficient accuracy could take advantage of the stretch induced in the ventricles by atrial contraction.

CONCLUSIONS

Basic feasibility of AKIS imaging for visualizing ablation lesions and chronic infarcts has been shown in an open-chested dog model for ablation lesions and in a transthoracic dog model for chronic infarcts. There is sufficient evidence for the approach to warrant additional studies going forward, particular in humans.

REFERENCES

Antonio EL, Santos AAD, Araujo SR, Bocalini DS, dos Santos L, Fenelon G, Franco MF, Tucci1 PJ. Left ventricle radio-frequency ablation in the rat: A new model of heart failure due to myocardial infarction homogeneous in size and low in mortality. J Card Fail 2009;156:540–548.

Bonow RO, Maurer G, Lee KL, Holly TA, Binkley PF, Desvigne-Nickens P, Drozdz J, Farsky PS, Feldman AM, Doenst T, Michler RE, Berman DS, Nicolau JC, Pellikka PA, Wrobel K, Alotti N, Asch FM, Favaloro LE, She L, Velazquez EJ, Jones RH, Panza JA. Myocardial viability and survival in ischemic left ventricular dysfunction. N Engl J Med 2011;364(17): 1617–1625.

Bouchard RR, Hsu SJ, Wolf PD, Trahey GE. *In vivo* cardiac, acoustic-radiation-force-driven, shear wave velocimetry. Ultrason Imaging 2009;313:201–213.

Byram BC, Holley G, Giannantonio DM, Trahey GE. 3-d phantom and in vivo cardiac speckle tracking using a matrix array and raw echo data. IEEE Trans Ultrason Ferroelectr Freq Contr 2010;574: 839–854.

Byram BC, Trahey GE, Palmeri M. Effect of prior probability quality on biased time-delay estimation. Ultrason Imaging 2012;342:65–80.

Byram BC, Trahey GE, Palmeri M. Bayesian speckle tracking. Part i: An implementable perturbation to the likelihood function for ultrasound displacement estimation. IEEE Trans Ultrason Ferroelectr Freq Contr 2013a;601:132–143.

Byram BC, Trahey GE, Palmeri M. Bayesian speckle tracking. Part ii: Biased ultrasound displacement estimation. IEEE Trans Ultrason Ferroelect Freq Contr 2013b;601:144–157.

Céspedes I, Huang Y, Ophir J, Spratt S. Methods for estimation of sub-sample time delays of digitized echo signals. Ultrason Imaging 1995;17:142–171.

Chen L, Housden RJ, Treece GM, Gee AH, Prager RW. A hybrid displacement estimation method for ultrasonic elasticity imaging. IEEE Trans Ultrason Ferroelectr Freq Control 2010;574:866–882.

Chen L, Treece GM, Lindop JE, Gee AH, Prager R. A quality-guided displacement tracking algorithm for ultrasonic elasticity imaging. Med Image Anal 2009;132:286–296.

Chik W, Barry M, Malchano Z, Wylie B, Pouliopoulos J, Huang K, Lu J, Thavapalachandran S, Robinson D, Saadat V, Thomas S, Ross D, Kovoor P, Thiagalingam A. In vivo evaluation of virtual electrode mapping and ablation utilizing a direct endocardial visualization ablation catheter. J Cardiovasc Electrophysiol 2012;231:88–95.

Chung ES, Leon AR, Tavazzi L, Sun JP, Nihoyannopoulos P, Merlino J, Abraham WT, Ghio S, Leclercq C, Bax JJ, Yu CM, Gorcsan J, Sutton SJ, De Sutter J, Murillo J. Results of the predictors of response to CRT (PROSPECT) trial. Circulation 2008;117(20): 2608–2616.

Cleland JG, Calvert M, Freemantle N, Arrow Y, Ball SG, Bonser RS, Chattopadhyay S, Norell MS, Pennell DJ, Senior R. The heart failure revascularisation trial (heart). Eur J Heart Fail 2011;132:227–233.

Couade M, Pernot M, Messas E, Bel A, Ba M, Hagege A, Fink M, Tanter M. In vivo quantitative mapping of myocardial stiffening and transmural anisotropy during the cardiac cycle. IEEE Trans Med Imaging 2011;302:295–305.

Earls JP, Ho VB, Foo TK, Castillo E, Flamm SD. Cardiac MRI: Recent progress and continued challenges. J Magn Reson Imaging 2002; 162:111–127.

Eyerly SA, Hsu SJ, Agashe SH, Trahey GE, Li Y, Wolf PD. An in vitro assessment of acoustic radiation force impulse imaging for visualizing cardiac radiofrequency ablation lesions. J Cardiovasc Electrophysiol 2010;21:557–563.

Giannantonio DM, Dumont DM, Trahey GE, Byram BC. Comparison of physiological motion filters for in vivo cardiac ARFI. Ultrason Imaging 2011;332:89–108.

Heimdal A, Stoylen A, Torp H, Skjaerpe T. Real-time strain rate imaging of the left ventricle by ultrasound. J Am Soc Echocardiogr 1998; 11(11):1013–1019.

Hsu SJ, Bouchard RR, Dumont DM, Ong CW, Wolf PD, Trahey GE. Novel acoustic radiation force impulse imaging methods for visualization of rapidly moving tissue. Ultrason Imaging 2009;313: 183–200.

Hsu SJ, Bouchard RR, Dumont DM, Wolf PD, Trahey GE. In vivo assessment of myocardial stiffness with acoustic radiation force impulse imaging. Ultrasound Med. Biol 2007;33(11):1706–1719.

Jasaityte R, Claus P, Teske AJ, Herbots L, Verheyden B, Jurcut R, Rademakers F, D'hooge J. The slope of the segmental stretch-strain relationship as a noninvasive index of LV inotropy. JACC Cardiovas Imaging 2013;64:419–428.

Kallel F, Ophir J. A least-squares strain estimator for elastography. Ultrason Imaging 1997;19:195–208.

Kanai H. Propagation of spontaneously actuated pulsive vibration in human heart wall and in vivo viscoelasticity estimation. IEEE Trans Ultrason Ferroelectr Freq Contr 2005;52:1931–1942.

Kim RJ, Fieno DS, Parrish TB, Harris K, Chen EL, Simonetti O, Bundy J, Finn JP, Klocke FJ, Judd RM. Relationship of MRI delayed contrast enhancement to irreversible injury, infarct age, and contractile function. Circulation 1999;100(19):1992–2002.

Klabunde RE. Cardiovascular physiology concepts. Baltimore, MD: Lippincott Williams & Wilkins; 2004.

Lankton S, Tannenbaum A. Localizing region-based active contours. IEEE Trans Image Process 2008;1711:2029–2039.

Loupas T, Powers JT, Gill RW. An axial velocity estimator for ultrasound blood flow imaging, based on a full evaluation of the Doppler equation by means of a two-dimensional autocorrelation approach. IEEE Trans Ultrason Ferroelectr Freq Contr 1995;42(4):672–688.

Lubinski MA, Emelianov SY, Raghavan KR, Yagle AE, Skovoroda AR, O'Donnell M. Lateral displacement estimation using tissue incompressibility. IEEE Trans Ultrason Ferroelectr Freq Contr 1996;43: 247–256.

Mor-Avi V, Lang RM, Badano LP, Belohlavek M, Cardim NM, Derumeaux G, Galderisi M, Marwick T, Nagueh SF, Sengupta PP, Sicari R, Smiseth OA, Smulevitz B, Takeuchi M, Thomas JD, Vannan M, Voigt JU, Zamorano JL. Current and evolving echocardiographic techniques for the quantitative evaluation of cardiac mechanics: ASE/EAE consensus statement on methodology and indications: Endorsed by the Japanese Society of Echocardiography. J Am Soc Echocardiogr 2011;243:277–313.

Nightingale K, Palmeri M, Trahey G. Analysis of contrast in images generated with transient acoustic radiation force. Ultrasound Med Biol 2006;321:61–72.

Nillesen MM, Lopata RGP, Gerrits IH, Kapusta L, Huisman HJ, Thijssen JM, de Korte CL. Segmentation of the heart muscle in 3-d pediatric echocardiographic images. Ultrasound Med Biol 2007;339:1453–1462.

Oh JK, Pellikka PA, Panza JA, Biernat J, Attisano T, Manahan BG, Wiste HJ, Lin G, Lee K, Miller FA, Stevens S, Sopko G, She L, Velazquez EJ. Core lab analysis of baseline echocardiographic studies in the stich trial and recommendation for use of echocardiography in future clinical trials. J Am Soc Echocardiogr 2012;253:327–336.

Pellikka PA, Nagueh SF, Elhendy AA, Kuehl CA, Sawada SG. American society of echocardiography recommendations for performance, interpretation, and application of stress echocardiography. J Am Soc Echocardiogr 2007;209:1021–1041.

Pennell DJ, Sechtem UP, Higgins CB, Manning WJ, Pohost GM, Rademakers FE, van Rossum AC, Shaw LJ, Yucel EK. Clinical indications for cardiovascular magnetic resonance (CMR): Consensus panel report. Eur Heart J 2004;25(21):1940–1965.

Pislaru C, Urban MW, Nenadic I, Greenleaf JF. Shearwave dispersion ultrasound vibrometry applied to in vivo myocardium. In: EMBC. 2009 Annual International Conference of the IEEE Engineering in Medicine and Biology Society, Vols. 1–20, 2009:2891–2894.

Provost J, Lee WN, Fujikura K, Konofagou EE. Electromechanical wave imaging of normal and ischemic hearts in vivo. IEEE Trans Med Imaging 2010;293:625–635.

Simonetti OP, Kim RJ, Fieno DS, Hillenbrand HB, Wu E, Bundy JM, Finn JP, Judd RM. An improved MR imaging technique for the visualization of myocardial infarction. Radiology 2001;2181:215–223.

Tanaka H, Nesser HJ, Buck T, Oyenuga O, Jánosi RA, Winter S, Saba S, Gorcsan J. Dyssynchrony by speckle-tracking echocardiography and response to cardiac resynchronization therapy: Results of the Speckle Tracking and Resynchronization (STAR) study. Eur Heart J 2010;31:1690–1700.

Urheim S, Edvardsen T, Torp H, Angelsen B, Smiseth OA. Myocardial strain by Doppler echocardiography validation of a new method to quantify regional myocardial function. Circulation 2000;102:1158–1164.

Varghese T, Ophir J. A theoretical framework for performance characterization of elastography: the strain filter. IEEE Trans Ultrason Ferroelectr Freq Control 1997;441:164–172.

Velazquez EJ. Myocardial imaging should not exclude patients with ischemic heart failure from coronary revascularization. Circ Cardiovasc Imaging 2012;52:271–279.

Walker W, Trahey G. A fundamental limit on the performance of correlation-based phase correction and flow estimation techniques. IEEE Trans Ultrason Ferroelectr Freq Contr 1994;41:644–654.

Williams RI, Payne N, Phillips T, D'hooge J, Fraser AG. Strain rate imaging after dynamic stress provides objective evidence of persistent regional myocardial dysfunction in ischaemic myocardium: regional stunning identified? Heart 2005;912:152–160.

Wissner E, Stevenson WG, Kuck KH. Catheter ablation of ventricular tachycardia in ischaemic and non-ischaemic cardiomyopathy: Where are we today? A clinical review. Eur Heart J 2012;33(12):1440–1450.

Zervantonakis IK, Fung-Kee-Fung SD, Lee WN, Konofagou EE. A novel, view-independent method for strain mapping in myocardial elastography: eliminating angle- and centroid-dependence. Phys Med Biol 2007;52(14):4063–4080.

Zwanenburg JJM, Gotte MJW, Kuijer JPA, Hofman MBM, Knaapen P, Heethaar RM, van Rossum AC, Marcus JT. Regional timing of myocardial shortening is related to prestretch from atrial contraction: Assessment by high temporal resolution MRI tagging in humans. Am J Physiol Heart Circ Physiol 2005;288(2):H787–H794.